Aalto University

Wu, Bingxue; Zhang, Jian; Yang, Zhi; Lu, Xuanlin; Zhao, Xin; Liu, Wen; Chen, Jiaxuan; Zhao, Yicheng; Li, Yongdan

Achieve a high electrochemical oxidation activity by a self-assembled cermet composite anode with low Ni content for solid oxide fuel cells

Achieve a high electrochemical oxidation activity by a self-assembled cermet composite anode with low Ni content for solid oxide fuel cells

Bingxue Wu[a,b], Jian Zhang[a,b], Zhi Yang[a,b], Xuanlin Lu[a,b], Xin Zhao[a,b], Wen Liu[a,b], Jiaxuan Chen[a,b], Yicheng Zhao[a,b*], Yongdan Li[a,b,c]

[a]State Key Laboratory of Chemical Engineering (Tianjin University), Tianjin Key Laboratory of Applied Catalysis Science and Technology, School of Chemical Engineering and Technology, Tianjin University, Tianjin, 300072, China
[b]Collaborative Innovation Center of Chemical Science and Engineering (Tianjin), Tianjin, 300072, China
[c]Department of Chemical and Metallurgical Engineering, Aalto University, Kemistintie 1, FI-00076 Aalto, Finland
*Email: zhaoyicheng@tju.edu.cn

Abstract

Ni-based cermets are the most widely used anode materials for solid oxide fuel cells. Reducing the content of Ni is beneficial to anode stability but usually unfavorable for the catalytic activity. In this study, Ni-Ce$_{0.8}$Sm$_{0.2}$O$_{2-\delta}$ anode with a low Ni content is synthesized through a polymer-directed evaporation induced self-assembly strategy. Ni distributes evenly in the anode, resulting in enlarged triple phase boundary region and improved reactivity of lattice oxygen in the oxide phase. The anode containing 5 wt.% Ni possesses the highest amounts of oxygen vacancies and Ce^{3+}/Ce^{4+} redox pairs that facilitates the charge transfer process, which is one of the rate-determining steps of anode reaction. Consequently, that anode shows the lowest polarization resistance of 0.014 Ω cm^2 at 700 ^{o}C, much lower than those of other Ni-based anodes prepared through conventional techniques such as impregnation and solid-mixing. With that anode, a single cell supported by a 480 µm-

thick $Ce_{0.8}Sm_{0.2}O_{2-\delta}$ electrolyte layer exhibit the maximum power density of 270 mW cm^{-2} at 700 °C. The anode also shows a promising stability.

Introduction

Solid oxide fuel cell (SOFC) is considered as a promising energy conversion device because of its high efficiency, environmental sustainability and wide fuel adaptability [1]. The high operating temperature (800-1000 $^{\circ}$C) of conventional SOFCs brings many challenges for their design and development, and lowering the operating temperature is crucial [2]. However, the charge transfer processes at the electrodes will be slowed down remarkably with the decrease of temperature, leading to depressed cell performance [3]. Developing electrode materials with high electrochemical catalytic activity in the intermediate temperature range (600-800 $^{\circ}$C) is essential for the practical application of SOFCs.

Nickel-based cermets such as Ni-yttria stabilized zirconia (YSZ) and Ni-doped ceria are the most widely used anode materials for SOFCs with high electrical conductivity and promising catalytic activity [4]. The content of Ni in conventional composite anodes is generally not less than 30 vol.% to achieve the percolation threshold for electronic conduction and sufficient active sites [5, 6]. Nonetheless, the high amount of Ni causes sintering at high temperatures as well as significant volume change during redox cycles, leading to poor mechanical stability and the failure of anode microstructure [7-10]. Various strategies have been proposed to overcome those issues. Han et al. [11] prepared a thin 50 wt.% Ni-50 wt.% YSZ anode layer on a thick porous YSZ support for a tubular SOFC, and no significant degradation in cell performance is observed after seven redox cycles. Kim et al. [12] deposited a 200 nm-thick 60 vol.% Ni-40 vol.% $Ce_{0.8}Sm_{0.2}O_{2-\delta}$ (SDC) anode layer on YSZ electrolyte via

reactive co-sputtering, and found that the stability of the anode is highly influenced by the oxygen partial pressure and the temperature during deposition. Another effective approach is to reduce the content of Ni in the composite anode. It is proved that by reducing the size of Ni particles, cermet anodes with low Ni contents can also possess high electronic conductivities [13, 14]. Park et al. [15] fabricated a thin Ni-$Ce_{0.9}Gd_{0.1}O_{2-\delta}$ (GDC) anode film with 2 vol.% Ni nanoparticles through pulsed laser deposition, the catalytic activity of which is comparable to conventional cermet anode with 40 vol.% Ni. The anode with extremely low Ni content also shows a remarkable stability with no performance degradation after 100 redox cycles at 600 °C. However, the high-cost and time-consuming deposition method is not suitable for large-scale application.

The decrease of Ni content in the composite anode not only favors the stability, but also strengthens the effects of the ceramic phase that also plays an important role in the electrochemical oxidation process of the fuels [16]. The catalytic activity of Ni-doped ceria is generally higher than that of Ni-YSZ anode mainly due to the Ce^{3+}/Ce^{4+} redox pair that facilitates the storage and release of oxygen [17, 18]. Huang et al. [19] found that the doping of Pr in SDC weakens the bonds between metal and oxygen atoms and thus facilitates the surface exchange and bulk diffusion of oxygen, resulting in a higher electrochemical oxidation kinetics. Similar results are obtained by doping La and Nd in SDC [20]. Gan et al. [21] prepared SDC with a three-dimensionally ordered macroporous structure, which exhibits a stronger interaction with Ni compared to bulk SDC. Accordingly, the reaction between lattice oxygen and

4

hydrogen adsorbed on Ni is accelerated, and the anode activity is improved significantly.

As a promising strategy to prepare cermet electrodes with metal nanocatalysts distributed uniformly, in situ exsolution of transition metal nanoparticles from oxide hosts has been intensively studied in recent years [22-26]. Tan et al. [27] incorporated 5 mol.% Ni in GDC through a sol-gel process, followed by in situ exsolution of 2 vol.% Ni nanoparticles in H_2. The exsolved Ni nanoparticles are strongly attached to GDC, yielding an enlarged triple phase boundary (TPB) and a strong interaction between Ni and GDC. The polarization resistance (R_p) of the anode is 1.04 Ω cm^2 at 650 ^{o}C. In 2020, Xiong et al. [28] developed a polymer-oriented evaporation induced self-assembly strategy to synthesize crystalline mesoporous TiO_2 with a large surface area and a high thermostability. Combining that process with in situ exsolution, we prepared Ni-SDC composite anode material with a low Ni content in this work. The anode with a homogeneous distribution of Ni shows a high catalytic activity and a promising stability in the intermediate temperature range. The electrochemical oxidation process at the anode is systematically investigated.

Experimental

Materials synthesis

x wt% Ni-Ce$_{0.8}$Sm$_{0.2}$O$_{2-\delta}$ (xNi-SDC, x = 3, 5, 10, 15) anode powders were synthesized through a polymer-directed evaporation induced self-assembly method [28]. Raw materials were purchased from Shanghai Aladdin Bio-Chem Technology Co., Ltd unless otherwise stated. Stoichiometric SmCl$_3$·6H$_2$O (99.99%), CeCl$_3$

(99.99%) and $NiCl_2 \cdot 6H_2O$ (99.9%) were dissolved in 1.67×10^3 mM deionized water to form a mixed solution with a total metal ion concentration of 33 mM. Then 35 mM CH_3COOH (99.8%), 12 mM HCl (37%) and 2.67 mM polyethylenimine (PEI, Shanghai Macklin Bio-Chem Technology Co., Ltd, Mw = 600, 99%) were added into the solution, followed by stirring for two hours until a transparent sol was formed. The sol was aged at 40 °C for 24 h and subsequently dried at 100 °C for another 24 h. The obtained precursor was calcined in the air at 700 °C for 5 h to form the anode powders, which were then reduced with H_2 at 700 °C for 2 h for characterization. For comparison, 5 wt.% $Ni-Ce_{0.8}Sm_{0.2}O_{2-\delta}$ was also prepared though an incipient-wetness impregnation process with $Ni(NO_3)_2 \cdot 6H_2O$ aqueous solution, which was marked as 5Ni-SDC(I).

Characterization

The phase structures of the anode powders before and after reduction were characterized with an X-ray diffractometer (XRD, Smartlab, Rigaku, Japan) at a scanning rate of $1°$ min^{-1}. The microstructure and morphology of the samples were observed using a scanning electron microscope (SEM, S-4800, Hitachi, Japan) and a transmission electron microscope (TEM, JEM-2100F, JEOL Inc., Japan) equipped with an energy dispersive x-ray (EDX) analyzer. The N_2 adsorption isotherms of the anode powders were measured using a Micromeritics ASAP 2460 analyzer. The specific surface area was determined based on the Brunauer-Emmett-Teller (BET) equation, and the pore-size distribution was evaluated according to the Barrett-Joyner-Halenda (BJH) method. Prior to the measurement, samples were evacuated

and degassed at 300 °C for 3 h. Hydrogen temperature-programmed reduction (H_2-TPR) of the anode powders were carried out using an Auto Chem II 2920 (Micromeritics, USA) in 10% H_2-90% Ar at a heating rate of 10 °C min^{-1} from room temperature to 800 °C. The surface chemical state of the samples were analyzed using an ESCALAB 250Xi X-ray photoelectron spectrometer (XPS, ThermoFischer, USA) using Al-Kα (hv = 1486.6 eV) as the X-ray source, and the binding energies were calibrated against the C 1s peak at 284.8 eV.

Electrochemical properties

The SDC electrolyte powder was pressed uniaxially at 300 MPa into pellets and then sintered at 1400 °C for 4 h in air [29]. The anode powder was mixed with an organic binder (V006, Heraeus Ltd.) to form a slurry. The slurry was screen-printed on both sides of the electrolyte pellet, and then calcined in air at 950 °C for 1 h to form a symmetrical cell. The geometrical area of the electrodes was 0.38 cm^2. Ag was applied on both sides of the cell as the current collector. The electrodes were reduced in H_2 at 700 °C for 2 h, and then the electrochemical impedance spectra (EIS) of the symmetric cells were recorded using an electrochemical workstation (VERSASTAT 3, Ametek) at 700 °C in the frequency range of 1 MHz - 0.01 Hz with an amplitude of 30 mV under various H_2 partial pressures (P_{H2}) with Ar as the balance gas.

Single cells were manufactured through a similar screen-printing procedure. The $La_{0.6}Sr_{0.4}Co_{0.2}Fe_{0.8}O_{3-\delta}$ (LSCF) cathode powder was synthesized via the glycine-nitrate combustion method [30, 31]. The anode layer was reduced in H_2 at 700 °C for 2 h, and then the performances of the cells were measured with dry H_2 (50 mL min^{-1},

STP) as the fuel and O_2 (10 mL min^{-1}, STP) as the oxidant gas.

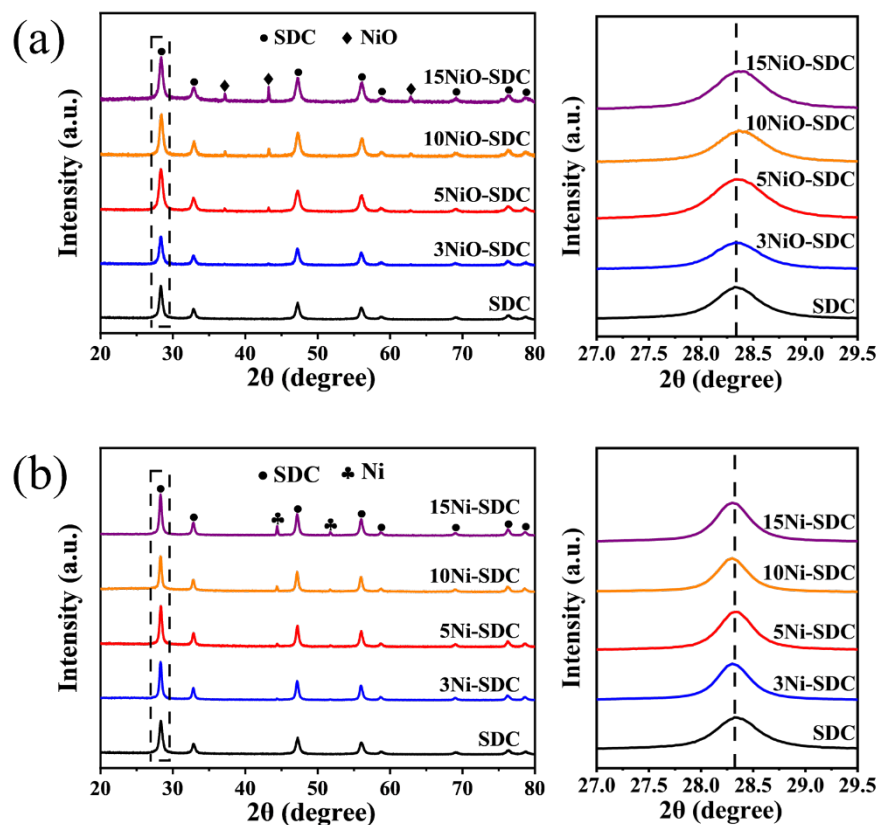## Results and discussion

Characterization

Figure 1. XRD patterns of the anode powders (a) before and (b) after reduction.

The XRD patterns of the anode powders before reduction (marked as xNiO-SDC) are shown in Figure 1a. The characteristic peaks of SDC phase with a cubic fluorite structure (JCPDS #75-0158) are observed, which shift to higher angles gradually with the increase of Ni content in the anode, indicating a slight shrinkage of the unit cells probably due to the partial incorporation of Ni^{2+} (0.69 Å) with a smaller radius compared with Ce^{4+} (0.87 Å). The peaks of NiO phase (JCPDS #89-7101) are also observed. After reduction, NiO in the anode is reduced to Ni (JCPDS #65-2865,

Figure 1b). Meanwhile, unlike the XRD results before reduction, the right-shift of the SDC peaks is not obvious, implying the exsolution of Ni incorporated in the SDC lattice after reduction.

The anode powders synthesized through the polymer-evaporation process before reduction all show a spongy morphology (Figure 2a-d), and their N_2 adsorption-desorption isotherms exhibit typical characteristic of mesoporous structures (Figure 3). The BET surface areas (S_{BET}) of the anodes are in the range of 16-21 $m^2\ g^{-1}$ (Table 1). The pore volumes and average pore diameters of the anodes are 0.054-0.061 $cm^3\ g^{-1}$ and 12.5-15.0 nm, respectively. A small amount of nanoparticles, probably NiO, can be observed on the surface of 15Ni-SDC, which are negligible on the surface of other anodes with lower Ni contents. For comparison, the surface nanoparticles are more obvious on 5Ni-SDC(I) (Figure 2e), indicating that the polymer-directed evaporation induced self-assembly technique is beneficial for the homogeneous distribution of Ni in the anode compared with the conventional impregnation process. 5Ni-SDC(I) anode shows the largest pore volume and average pore diameter of 0.107 $cm^3\ g^{-1}$ and 20.8 nm, respectively. Figure 4a shows the TEM image of 5Ni-SDC powder after reduction. The size of the nanocrystallites is about 10 nm. The (200) and (111) planes in SDC with interplanar spacings of 0.272 and 0.314 nm are observed in the HRTEM image (Figure 4b), as well as the (200) and (111) planes in Ni with lattice spacings of 0.176 and 0.203 nm, respectively. The STEM image with the EDX elemental mapping confirms the homogeneous distribution of Ni, Ce, Sm and O in the 5Ni-SDC anode (Figure 4c), suggesting a large TPB region.
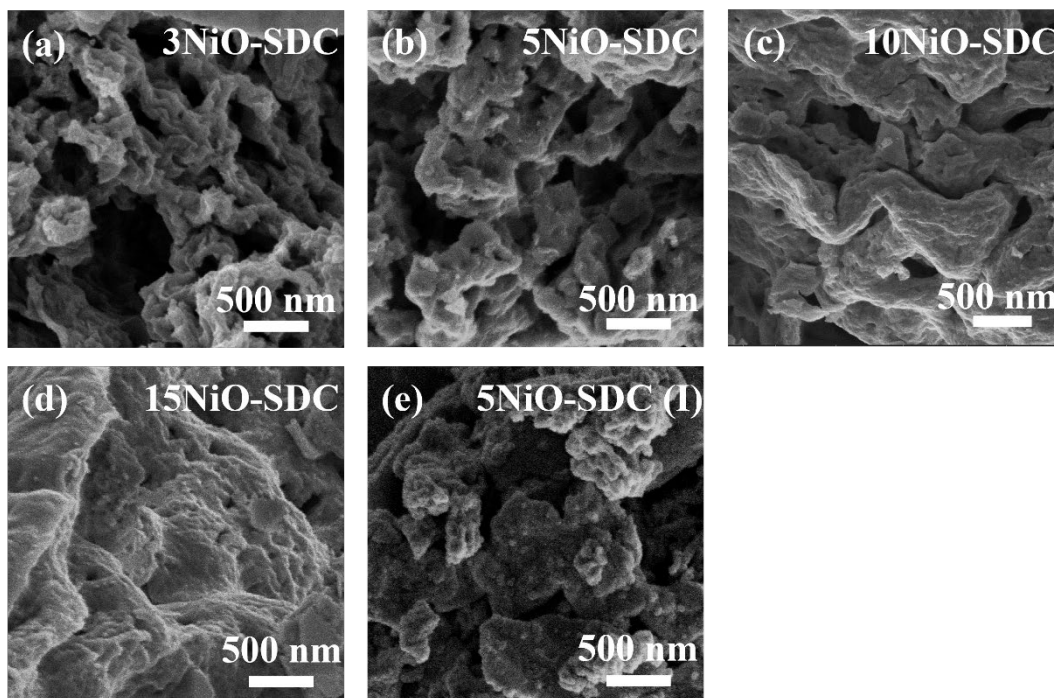
Figure 2. SEM images of anode powders before reduction: (a) 3NiO-SDC; (b) 5NiO-SDC; (c) 10NiO-SDC; (d) 15NiO-SDC; (e) 5NiO-SDC(I).
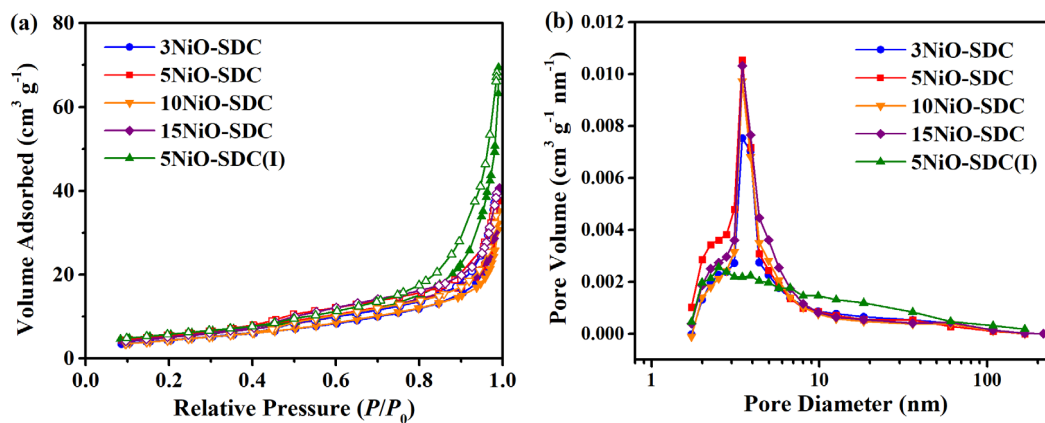

Figure 3. (a) Nitrogen adsorption-desorption isotherms and (b) pore size distributions of anode powders before reduction.

Table 1. Structural properties of anode materials

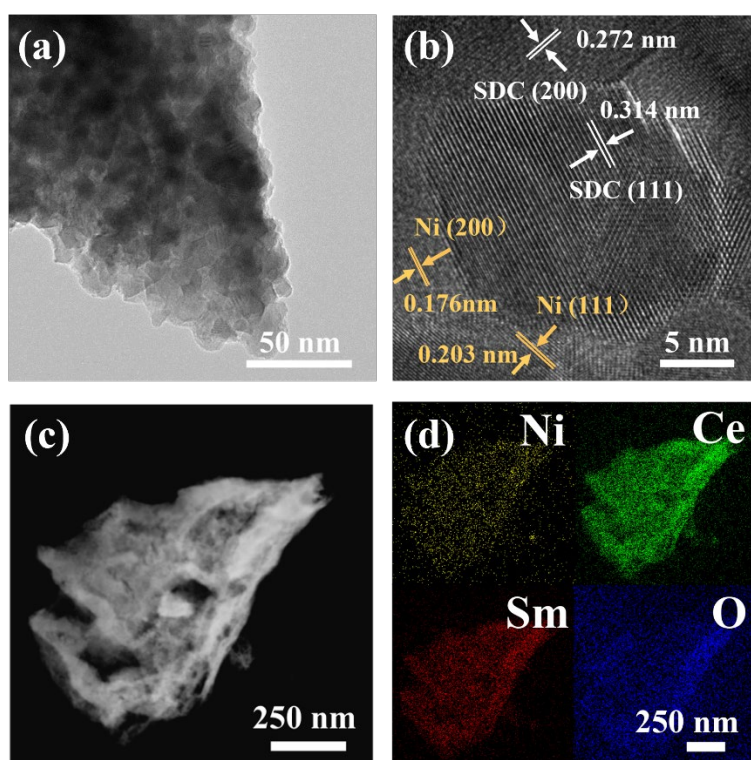| Anode	S_{BET} (m^2 g^{-1})	Total pore volume (cm^3 g^{-1})	Average pore diameter (nm)
3Ni-SDC	16.2	0.061	15.0
5Ni-SDC	20.9	0.057	10.8
10Ni-SDC	16.3	0.054	13.2
15Ni-SDC	19.1	0.060	12.5
5Ni-SDC(I)	20.6	0.107	20.8

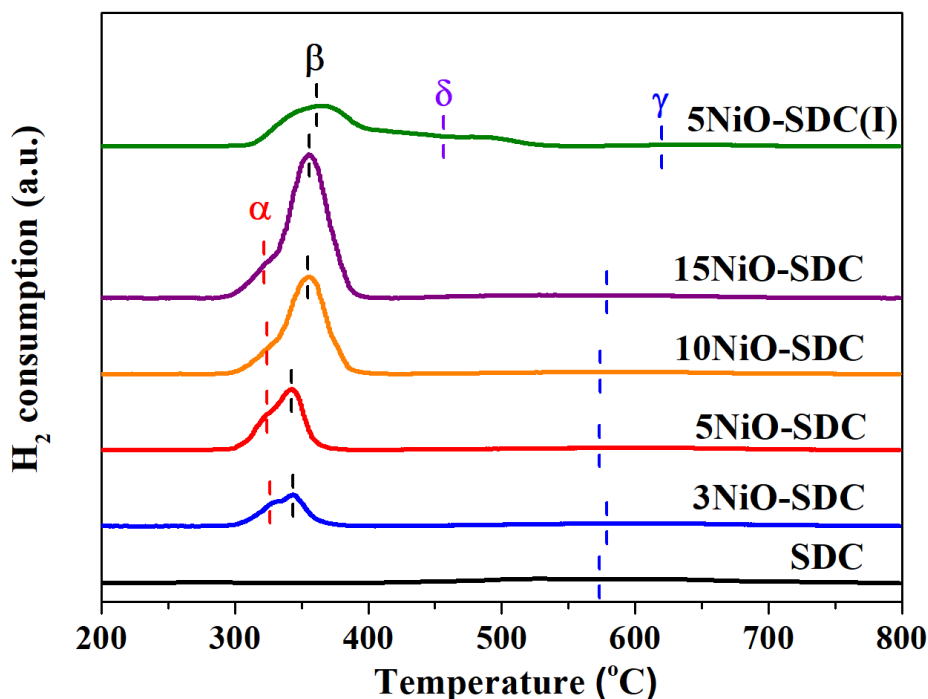Figure 4. (a) TEM image, (b) HRTEM image, (c) STEM image and (d) EDS elemental mappings of 5Ni-SDC powder after reduction.

Figure 5. H_2-TPR profiles of anode powders.

The H_2-TPR results of the anode powders are presented in Figure 5. A broad and weak H_2 consumption peak (γ peak) is observed in the temperature range from 400 to 800 °C in the profile of pure SDC attributed to the reduction of surface and bulk Ce^{4+} [32]. Another two peaks are found at lower temperatures in the TPR results of the NiO-SDC anode powders synthesized through the polymer-evaporation process. The reduction peaks are highly related to the size of Ni particles and the interaction between Ni and SDC phases [33-38]. The α peak at about 320 °C is attributed to the reduction of Ni species incorporated within SDC lattice and NiO on the surface or with smaller size. The β peak at about 350 °C is predominately assigned to the reduction of bulk NiO, which is usually overlapped with the reduction of the higher reducible Ce^{4+} near the Ni sites. The β peak moves to higher temperatures with the

increase of Ni content mainly due to the growth of NiO particles (Figure 2). The α

peak is not observed in the result of 5NiO-SDC(I) because of the lack of Ni in SDC

lattice and small NiO particles, and the β peak shifts to higher temperature compared

with 5NiO-SDC. In addition, the H_2 consumption in 400-500 °C (δ peak) corresponds

to the reduction of larger NiO particles observed in the SEM image (Figure 2e), which

is accompanied by the reduction of Ce^{4+}. Compared with NiO particles aggregated on

the surface of the composite anode prepared through impregnation, NiO in the anode

synthesized via the polymer-evaporation process shows a homogeneous distribution

with a smaller size, which not only reduces the reduction temperature of NiO, but also

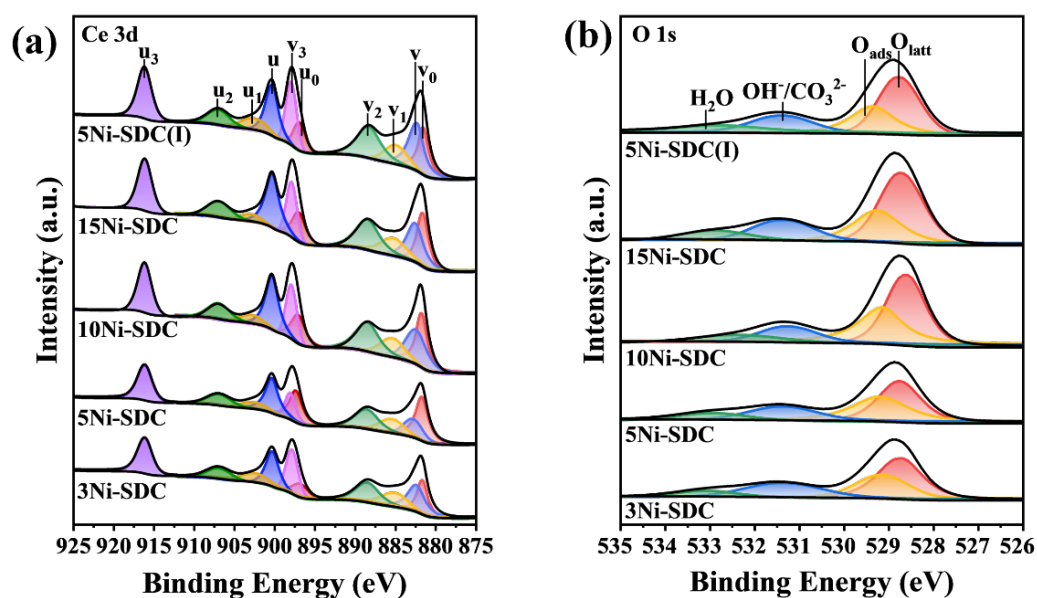facilitates the removal of lattice oxygen in SDC by hydrogen adsorbed on adjacent

Ni.

Figure 6. XPS spectra of (a) Ce 3d and (b) O 1s of the reduced samples.

The Ce 3d XPS curves of the anodes after reduction can be deconvoluted into ten peaks (Figure 6a). The u_0-v_0 and u_1-v_1 peaks are attributed to Ce^{3+}, while the u-v, u_2-v_2 and u_3-v_3 doublets are ascribed to Ce^{4+} [39-41]. The content of Ce^{3+} in 3Ni-SDC is 30.2%, which increases to 39.7% in 5Ni-SDC (Table 2). Further increase of Ni in the anode leads to less Ce^{3+}. Meanwhile, the content of Ce^{3+} in 5Ni-SDC is higher than that in 5Ni-SDC(I) probably due to the strong interaction between Ni and SDC in the polymerization synthesized anode, consistent with the H_2-TPR results (Figure 5). The O 1s spectra of the reduced samples are shown in Figure 6b. The peaks at about 528.5 eV is attributed to lattice oxygen (O_{latt}), while the peaks at 529.4, 531.5 and 533.0 eV can be assigned to oxygen (O_{ads}), oxygen species (OH^-/CO_3^{2-}) and H_2O adsorbed on surface oxygen vacancies (O_V), respectively [42, 43]. 5Ni-SDC has the lowest amount of O_{latt}, consistent with its highest Ce^{3+} content.

Table 2. Contents of Ce and O species on the surface of the reduced anode powders analyzed by XPS.

Sample	Ce (%)		O (%)			
	Ce^{3+}	Ce^{4+}	O_{latt}	O_{ads}	OH^-/CO_3^{2-}	H_2O
3Ni-SDC	30.2	69.8	41.1	24.7	23.9	10.3
5Ni-SDC	39.7	60.3	38.3	29.9	19.2	12.6
10Ni-SDC	31.2	68.8	44.4	29.8	13.8	12.0
15Ni-SDC	29.0	71.0	46.3	24.1	18.5	11.1
5Ni-SDC(I)	29.1	70.9	46.5	25.1	19.1	9.30

Electrochemical properties

The EIS plots of the symmetric cells with different anodes at 700 ℃ under various P_{H2} are presented in Figure 7a. The ohmic resistances of the cells are deducted for better comparison, and the arcs are fitted with a simplified equivalent circuit of $(R_HCPE_H)(R_LCPE_L)$. R_H and R_L are the polarization resistances of the anodes in the high frequency (HF) and low frequency (LF) ranges, respectively, and CPE_H and CPE_L are the corresponding constant phase elements. The R_P of 3Ni-SDC anode in pure hydrogen is 0.016 Ω cm^2, which decreases slightly to 0.014 Ω cm^2 when the content of Ni increases to 5 wt.%, while further addition of Ni leads to a larger R_P. The catalytic activity of 5Ni-SDC anode is much higher than that of the impregnated anode with the same Ni content. Furthermore, the R_L of the anodes are generally one order of magnitude higher than R_H, indicating that the anode reaction is dominated by the low-frequency process.

Typically, R_P and P_{H2} exhibit a power law relationship ($R_P \propto P_{H2}{}^n$) [21, 26, 44, 45]. As shown in Figure 7b, R_H change negligibly with the variation of P_{H2} (n_H is approximately 0), implying that the rate-determining step (RDS) in the high-frequency process does not involve hydrogen species, probably the transfer of oxygen ions in the anode. In clear contrast, R_L of all the anodes increase remarkably with the decrease of P_{H2} (Figure 7c). The value of n_L is about -1 when the content of Ni in the anode is lower than 5 wt.%, indicating that the RDS of the low-frequency process is the dissociative adsorption of H$_2$ due to the small amount of Ni active sites. With the increase of Ni content, the dissociative adsorption of H$_2$ on the surface of the anode

becomes faster. On the other hand, the concentrations of O_V and Ce^{3+}/Ce^{4+} redox pairs

both decrease (Table 2), leading to a slower kinetics of charge transfer between the H

species adsorbed on Ni and the adjacent oxygen (Figure 5), and thus n_L and R_L both
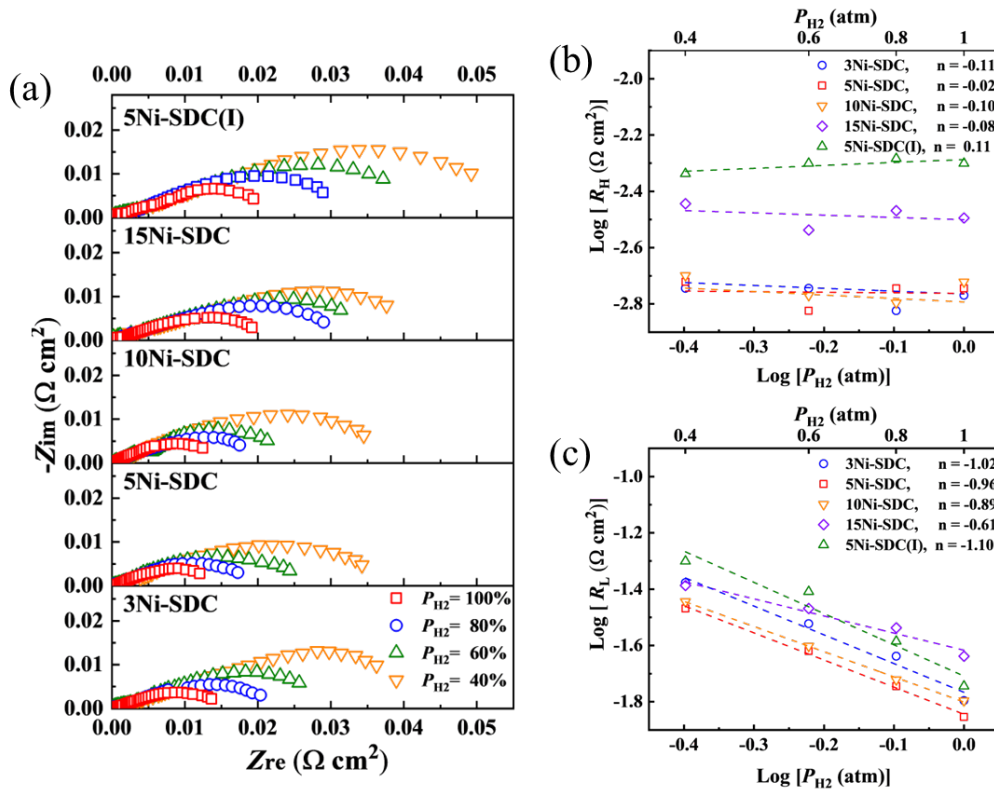
increase.

Figure 7. (a) Impedance spectra of the half symmetric cells with different anodes

under various P_{H2} at 700 °C; (b) R_H of the anodes under various P_{H2}; (c) R_L of the

anodes under various P_{H2}.

The cross-sectional SEM image of the single cell with 5NiO-SDC anode is

shown in Figure 8a. The porous anode and cathode layers adhere tightly to the 480

μm-thick dense SDC electrolyte layer with distinct interfaces. The thicknesses of the

anode and cathode layers are both 45 μm. Figure 8b presents the current-voltage (*I-V*) and current-power (*I-P*) characteristics of the cells with various anodes at 700 °C. The open circuit voltages (OCVs) of the cells are in the range of 0.85-0.90 V, which are lower than the theoretical value (about 1.0 V) due to the electronic conduction through the SDC electrolyte layer caused by the partial reduction of Ce^{4+} to Ce^{3+}. The cell with 5Ni-SDC anode shows the highest maximum power density (P_{max}) of 270 mW cm^{-2} attributed to the highest catalytic activity of the anode. In comparison, the P_{max} of the cell with 5Ni-SDC(I) anode is only 170 mW cm^{-2}, demonstrating the superiority of the anode synthesized through the polymer-evaporation process. The EIS curves of the single cells with various anodes at 700 °C are shown in Figure 8c. Since the cathode and electrolyte are identical for all the cells, the differences in the EIS results could be attributed only to the differences of the anodes. The ohmic resistances of all the cells are similar, while the R_P shows an order of 5Ni-SDC < 10Ni-SDC < 3Ni-SDC < 15Ni-SDC <5Ni-SDC(I), consistent with the results of the symmetric cells (Figure 7a).
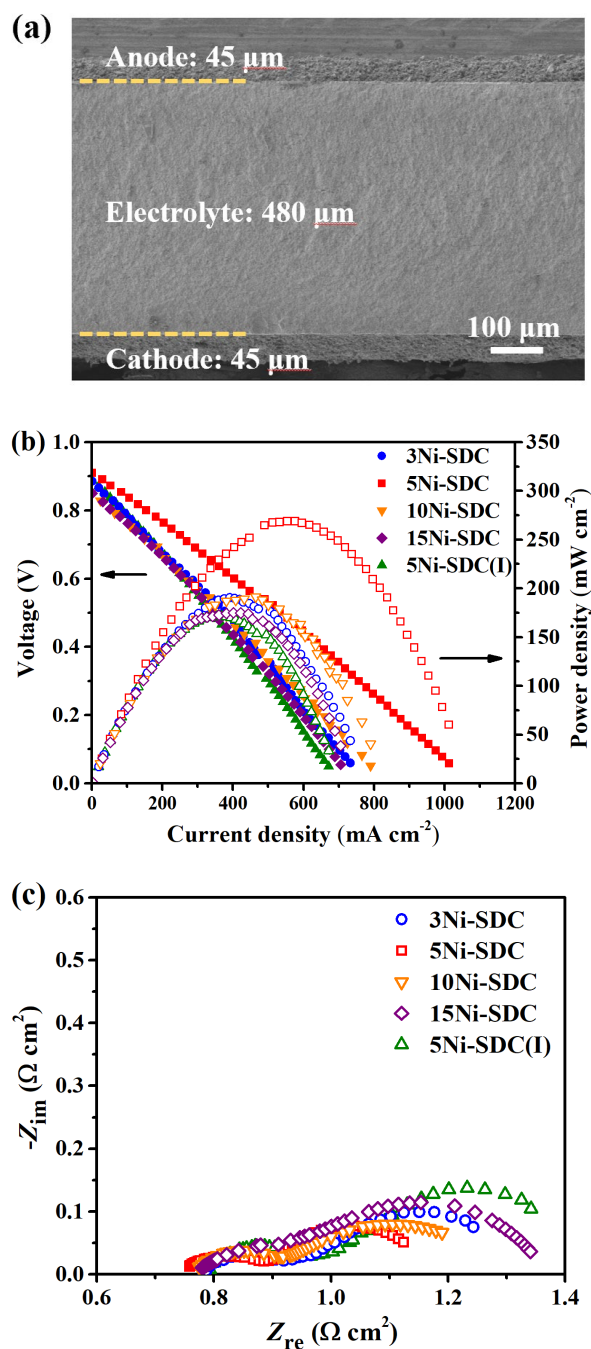
Figure 8. (a) Cross-sectional SEM image of the cell with 5NiO-SDC anode; (b) *I-V* and *I-P* curves and (c) EIS results of single cells with various anodes at 700 °C.

Finally, the anode developed in this work is compared with the conventional solid-mixed 50 vol.% Ni -50 vol.% SDC (50Ni-50SDC) anode. As shown in Figure 9a, the reduction peak of NiO in 50Ni-50SDC is significantly shifted to a higher

temperature compared with that in 5Ni-SDC, indicating the agglomeration of NiO in 50Ni-50SDC with a much larger particle size. Besides, the H_2 consumption peak in the range of 450-650 °C can be assigned to the reduction of Ce^{4+} not adjacent to Ni in 50Ni-50SDC, implying a lower activity of lattice oxygen. The R_P of 50Ni-50SDC anode (with the Ag paste as the current collector) is about 0.025 Ω cm^2 at 700 °C (Figure 9b), which is among the best of Ni-based cermet anodes with high Ni contents [46-49]. Though having a much lower content of Ni, 5Ni-SDC anode shows a remarkably improved kinetics attributed to the enhancement of the oxygen activity. Therefore, the cell with 5Ni-SDC anode shows a much higher P_{max} compared to the one with 50Ni-50SDC anode (Figure 9c). Meanwhile, 5Ni-SDC anode exhibits a stable R_P within 100 hours (Figure 9d). It is noteworthy that the electronic conductivity of the cermet anode with a low metal content is inevitably depressed to some extent, and its applicability in thick anode support layer is still uncertain. Nevertheless, the highly catalytic composite material synthesized through the polymer-evaporation process with a uniform distribution of Ni demonstrates its potential as an effective anode function layer [27].
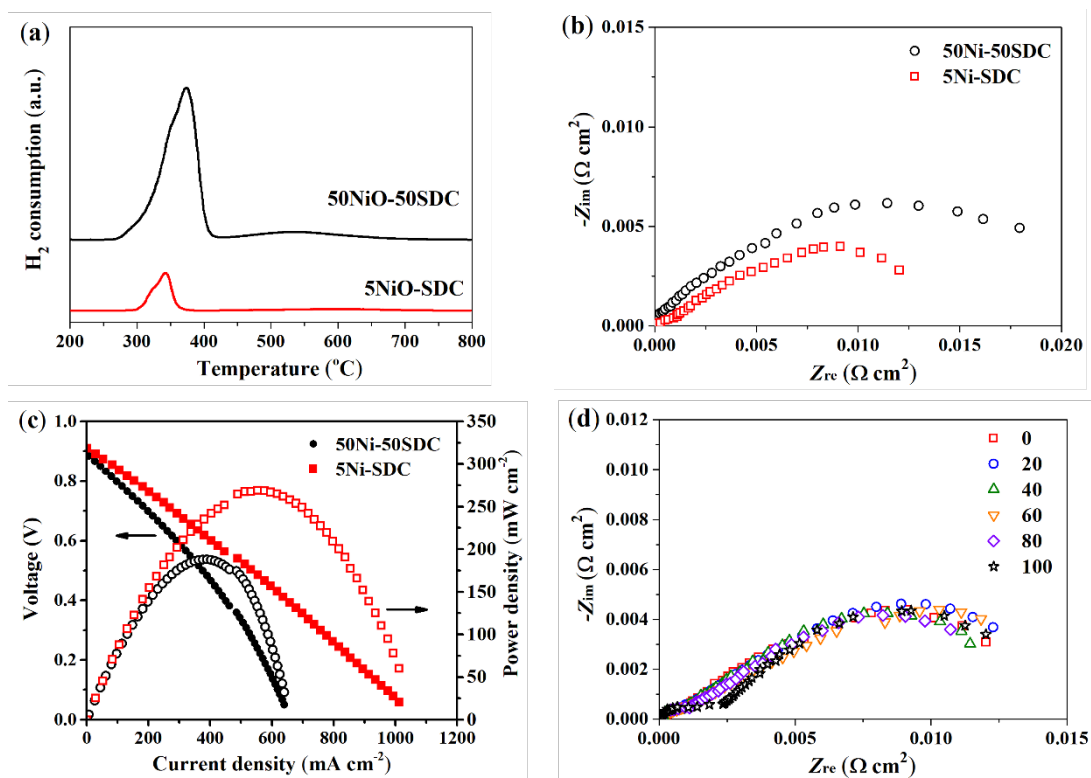
Figure 9. (a) H$_2$-TPR profiles of anode powders; (b) Impedance spectra of the half symmetric cells with different anodes at 700 °C; (c) I-V and I-P curves of single cells with different anodes at 700 °C; (d) Impedance spectra of the half symmetric cell with 5Ni-SDC anode at 700 °C within 100 hours.

Conclusion

In this work, Ni-SDC cermet anode with a low Ni content is synthesized through a polymer-directed evaporation induced self-assembly approach. Compared with composite anodes prepared via conventional techniques such as impregnation, the anode synthesized through the polymer-evaporation process shows a uniform distribution of Ni, resulting in a smaller particle size and a lower reduction temperature of NiO. Meanwhile, the homogeneous distribution of Ni also enlarges the TPB region and improves the reactivity of lattice oxygen in SDC. With the

increase of Ni content in the anode, the RDS of the anode process is changed gradually from the dissociative adsorption of H_2 to the surface reaction of oxygen species with adsorbed H. The anode containing 5 wt.% Ni possesses the highest concentrations of O_V and Ce^{3+}/Ce^{4+} redox pairs that facilitates the charge transfer process, and thus shows the lowest R_P of 0.014 Ω cm^2 at 700 ^{o}C. A single cell supported by a 480 μm-thick SDC electrolyte layer using that anode shows the highest P_{max} of 270 mW cm^{-2} at 700 ^{o}C. The results demonstrate that the self-assembled cermet with a low Ni content is a promising anode material for SOFCs.

Acknowledgements

Statements and Declarations

The authors declare no competing financial or non-financial interests.

References

1.   Hesami H, Borji M, Rezapour J (2021) A comprehensive three-dimensional modeling of an

internal reforming planar solid oxide fuel cell with different interconnect designs. J Solid State Electr 25(10-11):2639-2664.

2. Fasquelle D, Chi Z, Belakry S (2022) Impregnation of gadolinium-doped ceria backbone electrodes modified by addition of pore-formers for SOFC application. J Solid State Electr 27(3):695-703.

3. Sciazko A, Miyahara K, Komatsu Y, Shimura T, Jiao Z, Shikazono N (2019) Influence of initial powder morphology on polarization characteristics of nickel/gadolinium-doped-ceria solid oxide fuel cells electrode. J Electrochem Soc 166(2):F44-F52.

4. Ao G, Yan Y, Zhao P, Pan Z, Lv Z, Wang Z (2022) Enhanced redox and reoxidation tolerances of $Ce_{0.8}Gd_{0.2}O_{1.9}$ electrolyte for Ni cermet anodes in single-chamber SOFCs. J Solid State Electr 26(3):865-873.

5. Xu Q, Guo Z, Xia L, He Q, Li Z, Temitope Bello I, Zheng K, Ni M (2022) A comprehensive review of solid oxide fuel cells operating on various promising alternative fuels. Energy Convers Manage 253:115175.

6. Shaikh SPS, Muchtar A, Somalu MR (2015) A review on the selection of anode materials for solid-oxide fuel cells. Renewable Sustainable Energy Rev 51:1-8.

7. Fang X, Lin Z (2018) Numerical study on the mechanical stress and mechanical failure of planar solid oxide fuel cell. Appl Energy 229:63-68.

8. Nerat M (2020) A model of solid oxide fuel cell degradation on a microstructural level. Appl Sci 10(6):1906.

9. Komatsu Y, Sciazko A, Suzuki Y, Ouyang Z, Jiao Z, Shikazono N (2021) Operando observation of patterned nickel-gadolinium doped ceria solid oxide fuel cell anode. J Power Sources 516:230670.

10. Sreedhar I, Agarwal B, Goyal P, Agarwal A (2020) An overview of degradation in solid oxide fuel cells-potential clean power sources. J Solid State Electr 24(6):1239-1270.

11. Han Z, Dong H, Yang Y, Yang Z (2022) Achieving robust redox stability of SOFC through Ni-YSZ anode layer thinning and inert support mechanical compensation. ACS Appl Energy Mater 5(5):5822-5829.

12. Kim T, Kim HJ, Go D, Shin JW, Yang BC, Cho GY, Gür TM, An J (2022) Reactive sputtered Ni-SDC cermet alloy anode for low-temperature solid oxide fuel cell. J Alloys Compd 924:166332.

13. Jasinski P, Suzuki T, Petrovsky V, Anderson HU (2005) Nanocomposite nickel ceria cermet with low nickel content for anode supported SOFCs. Electrochem Solid-State Lett 8(4):A219-A221.

14. Weng X, Brett D, Yufit V, Shearing P, Brandon N, Reece M, Yan H, Tighe C, Darr JA (2010) Highly conductive low nickel content nano-composite dense cermets from nano-powders made via a continuous hydrothermal synthesis route. Solid State Ionics 181(17-18):827-834.

15. Park JH, Lee JH, Yoon KJ, Kim H, Ji HI, Yang S, Park S, Han SM, Son JW (2021) A nanoarchitectured cermet composite with extremely low Ni content for stable high-performance solid oxide fuel cells. Acta Mater 206:116580.

16. Choolaei M, Cai Q, Horri BA (2021) Green synthesis and characterisation of nanocrystalline NiO-GDC powders with low activation energy for solid oxide fuel cells. Ceram Int 47(23):32804-32816.

17. Jaiswal N, Tanwar K, Suman R, Kumar D, Upadhyay S, Parkash O (2019) A brief review on

ceria based solid electrolytes for solid oxide fuel cells. J Alloys Compd 781:984-1005.

18. Gautam M, Ahuja A, Sinha A, Sharma J, Patro PK, Venkatasubramanian A (2020) Synthesis and characterization of gadolinium-doped ceria and barium cerate-based composite electrolyte material for IT-SOFC. Bull Mater Sci 43(1):1-9.

19. Huang Z, Fan L, Hou N, Gan T, Gan J, Zhao Y, Li Y (2020) Improved activity of oxygen in Ni–$Ce_{0.8}Sm_{0.2}O_{2-\delta}$ anode for solid oxide fuel cell with Pr doping. J Power Sources 451:227809.

20. Zhang Y, Huang Z, Gan T, Hou N, Fan L, Zhou X, Gao G, Li J, Zhao Y, Li Y (2021) Cu-$Ce_{0.8}Sm_{0.2}O_{2-\delta}$ anode for electrochemical oxidation of methanol in solid oxide fuel cell: Improved activity by La and Nd doping. Solid State Ionics 369:115728.

21. Gan T, Fan X, Liu Y, Wang C, Mei H, Fan L, Hou N, Zhao Y, Li Y (2020) A highly active Ni/$Ce_{0.8}Sm_{0.2}O_{1.9}$ anode catalyst with a three-dimensionally ordered macroporous structure for solid oxide fuel cells. J Mater Chem A 8(16):7792-7800.

22. Zhang SL, Wang H, Yang T, Lu MY, Li CX, Li CJ, Barnett SA (2020) Advanced oxygen-electrode-supported solid oxide electrochemical cells with $Sr(Ti,Fe)O_{3-\delta}$-based fuel electrodes for electricity generation and hydrogen production. J Mater Chem A 8(48):25867-25879.

23. Zhang Y, Xu Y, Gan L (2021) Exsolved metallic iron nanoparticles in perovskite cathode to enhance CO2 electrolysis. J Solid State Electr 26(2):409-417..

24. Hou N, Yao T, Li P, Yao X, Gan T, Fan L, Wang J, Zhi X, Zhao Y, Li Y (2019) A-site ordered double perovskite with in situ exsolved core-shell nanoparticles as anode for solid oxide fuel cells. ACS Appl Mater Interfaces 11(7):6995-7005.

25. Zhu T, Troiani HE, Mogni LV, Han M, Barnett SA (2018) Ni-substituted $Sr(Ti,Fe)O_3$ SOFC anodes: achieving high performance via metal alloy nanoparticle exsolution. Joule 2(3):478-496.

26. Osinkin DA, Antonova EP, Shubin KS, Bogdanovich NM (2021) Influence of nickel exsolution on the electrochemical performance and rate-determining stages of hydrogen oxidation on $Sr_{1.95}Fe_{1.4}Ni_{0.1}Mo_{0.5}O_{6-\delta}$ promising electrode for solid state electrochemical devices. Electrochim Acta 369:137673.

27. Tan J, Lee D, Ahn J, Kim B, Kim J, Moon J (2018) Thermally drivenin situexsolution of Ni nanoparticles from (Ni, Gd)CeO_2 for high-performance solid oxide fuel cells. J Mater Chem A 6(37):18133-18142.

28. Xiong H, Zhou H, Qi C, Liu Z, Zhang L, Zhang L, Qiao ZA (2020) Polymer-oriented evaporation induced self-assembly strategy to synthesize highly crystalline mesoporous metal oxides. Chem Eng J 398:125527.

29. Gan T, Ding G, Chen B, Zhi X, Li P, Yao X, Hou N, Fan L, Zhao Y, Li Y (2019) Effects of manganese oxides on the activity and stability of Ni-$Ce_{0.8}Sm_{0.2}O_{1.9}$ anode for solid oxide fuel cells with methanol as the fuel. Catal Today 330:222-227.

30. Li J, Fan L, Hou N, Zhao Y, Li Y (2022) Solid oxide fuel cell with a spin-coated yttria stabilized zirconia/gadolinia doped ceria bi-layer electrolyte. RSC Adv 12(21):13220-13227.

31. SA AM, Raharjo J, Anwar M, Khaerudini DS, Muchtar A, Spiridigliozzi L, Somalu MR (2020) Carbonate-based lanthanum strontium cobalt ferrite (LSCF)-samarium-doped ceria (SDC) composite cathode for low-temperature solid oxide fuel cells. Appl Sci 10(11):3761.

32. Jurado L, Papaefthimiou V, Thomas S, Roger AC (2021) Low temperature toluene and phenol abatement as tar model molecules over Ni-based catalysts: Influence of the support and the

synthesis method. Appl Catal B 297:120479.

33. Zhou R, Mohamedali M, Ren Y, Lu Q, Mahinpey N (2022) Facile synthesis of multi-layered nanostructured Ni/CeO_2 catalyst plus in-situ pre-treatment for efficient dry reforming of methane. Appl Catal B 316:121696.

34. Bian Z, Chan YM, Yu Y, Kawi S (2020) Morphology dependence of catalytic properties of Ni/CeO_2 for CO_2 methanation: A kinetic and mechanism study. Catal Today 347:31-38.

35. Cesario MR, Souza GS, Loureiro FJA, Araújo AJM, Grilo JPF, Aouad S, Tidahy HL, Macedo DA, Fagg DP, Gennequin C, Abi-Aad E (2021) Synthesis of Co–Ni and Cu–Ni based-catalysts for dry reforming of methane as potential components for SOFC anodes. Ceram Int 47(23):33191-33201.

36. Escudero MJ, Valero C, Cauqui MÁ, Goma D, Yeste MP (2022) Ni-Ce-ZrO_2 system as anode material for direct internal reforming biogas solid oxide fuel cells. Fuel 322:124247.

37. Chagas CA, Souza EF, Manfro RL, Landi SM, Souza MMVM, Schmal M (2016) Copper as promoter of the NiO–CeO_2 catalyst in the preferential CO oxidation. Appl Catal B 182:257-265.

38. Torknik FS, Keyanpour-Rad M, Maghsoudipour A, Choi GM (2014) Effect of microstructure refinement on performance of $Ni/Ce_{0.8}Gd_{0.2}O_{1.9}$ anodes for low temperature solid oxide fuel cell. Ceram Int 40(1):1341-1350.

39. Zhou G, Liu H, Cui K, Jia A, Hu G, Jiao Z, Liu Y, Zhang X (2016) Role of surface Ni and Ce species of Ni/CeO_2 catalyst in CO_2 methanation. Appl Surf Sci 383:248-252.

40. Zhao X, Li H, Zhang J, Shi L, Zhang D (2016) Design and synthesis of $NiCe@m$-SiO_2 yolk-shell framework catalysts with improved coke- and sintering-resistance in dry reforming of methane. Int J Hydrogen Energy 41(4):2447-2456.

41. Hartmann P, Brezesinski T, Sann J, Lotnyk A, Eufinger JP, Kienle L, Janek J (2013) Defect chemistry of oxide nanomaterials with high surface area: Ordered mesoporous thin films of the oxygen storage catalyst CeO_2-ZrO_2. ACS Nano 7(4):2999–3013.

42. Zhu Y, Zhou W, Yu J, Chen Y, Liu M, Shao Z (2016) Enhancing electrocatalytic activity of perovskite oxides by tuning cation deficiency for oxygen reduction and evolution reactions. Chem Mater 28(6):1691-1697.

43. Zhang X, Pei C, Chang X, Chen S, Liu R, Zhao ZJ, Mu R, Gong J (2020) FeO_6 octahedral distortion activates lattice oxygen in perovskite ferrite for methane partial oxidation coupled with CO_2 splitting. J Am Chem Soc 142(26):11540-11549.

44. Zhi X, Gan T, Hou N, Fan L, Yao T, Wang J, Zhao Y, Li Y (2019) ZnO-promoted surface diffusion on NiO-$Ce_{0.8}Sm_{0.2}O_{1.9}$ anode for solid oxide fuel cell. J Power Sources 423:290-296.

45. Hou N, Gan J, Yan Q, Zhao Y, Li Y (2022) Improved electrochemical oxidation kinetics of $La_{0.5}Ba_{0.5}FeO_{3-\delta}$ anode for solid oxide fuel cells with fluorine doping. J Power Sources 521:230932.

46. Park BK, Scipioni R, Cox D, Barnett SA (2020) Enhancement of Ni-$(Y_2O_3)_{0.08}(ZrO_2)_{0.92}$ fuel electrode performance by infiltration of $Ce_{0.8}Gd_{0.2}O_{2-\delta}$ nanoparticles. J Mater Chem A 8(7):4099-4106.

47. Athanasiou M, Niakolas DK, Bebelis S, Neophytides SG (2020) Steam effect on gerischer impedance response of a Ni/GDC|YSZ|LSM fuel cell anode. J Power Sources 448:227404.

48. Grosselindemann C, Russner N, Dierickx S, Wankmüller F, Weber A (2021) Deconvolution of gas diffusion polarization in Ni/gadolinium-doped ceria fuel electrodes. J Electrochem Soc

168(12):124506.

49.   Osinkin DA (2020) Complementary effect of ceria on the hydrogen oxidation kinetics on Ni-$Ce_{0.8}Sm_{0.2}O_{2-\delta}$ anode. Electrochim Acta 330:135257.